AIAA JOURNAL
Vol. 48, No. 12, December 2010

Prediction of Broadband Shock-Associated Noise Using Reynolds-Averaged Navier–Stokes Computational Fluid Dynamics

Philip J. Morris*
Pennsylvania State University, University Park, Pennsylvania 16803
and
Steven A. E. Miller†
NASA Langley Research Center, Hampton, Virginia 23681

DOI: 10.2514/1.J050560

Broadband shock-associated noise is a component of jet noise generated by supersonic jets operating offdesign. It is characterized by multiple broadband peaks and dominates the total noise at large angles to the jet downstream axis. A new model is introduced for the prediction of broadband shock-associated noise that uses the solution of the Reynolds-averaged Navier–Stokes equations. The noise model is an acoustic analogy based on the linearized Euler equations. The equivalent source terms depend on the product of the fluctuations associated with the jet's shock-cell structure and the turbulent velocity fluctuations in the jet shear layer. The former are deterministic and are obtained from the Reynolds-averaged Navier–Stokes solution. A statistical model is introduced to describe the properties of the turbulence. Only the geometry and operating conditions of the nozzle need to be known to make noise predictions. This overcomes the limitations and empiricism present in previous broadband shock-associated noise models. Results for various axisymmetric circular nozzles and a rectangular nozzle operating at various conditions are compared with experimental data to validate the model.

Nomenclature

D	=	jet exit diameter
D_j	=	fully expanded jet exit diameter
f_i^a	=	unsteady force associated with speed-of-sound fluctuations
f_i^v	=	unsteady force associated with velocity fluctuations
K	=	turbulent kinetic energy
k_1	=	axial wave number
l	=	axial length scale of turbulence
$l_\perp$	=	cross-stream turbulent length scale
M_d	=	nozzle design Mach number
M_j	=	fully expanded jet Mach number
NPR	=	nozzle total pressure ratio
p_o	=	total pressure
p_∞	=	ambient pressure
p'	=	pressure fluctuation
R	=	radial distance to observer in spherical coordinates
R^v	=	two-point cross-correlation of turbulent velocity fluctuations $(\mathbf{y}, \boldsymbol{\eta}, \tau)$
R^v_{nm}	=	two-point cross-correlation of broadband shock-associated noise source term $(\mathbf{y}, \boldsymbol{\eta}, \tau)$
r	=	radial distance in cylindrical coordinates
S	=	spectral density $(\mathbf{x}, \omega)$
TTR	=	nozzle total temperature ratio
T_o	=	total temperature
T_∞	=	ambient temperature
$\bar{u}_c$	=	axial convection velocity
v_i	=	Cartesian velocity components in the x_i directions
a	=	local speed of sound
γ	=	ratio of specific heats
ε	=	viscous dissipation rate
ζ	=	separation in the x_3 direction
$\boldsymbol{\eta}$	=	separation vector
η	=	separation in the x_2 direction
θ	=	dilatation rate fluctuation
θ	=	polar angle of observer
ξ	=	separation in the x_1 direction
π	=	logarithm of the pressure $(\mathbf{x}, t)$
π_g^n, v_{gi}^n	=	periodic vector Green's function $(\mathbf{x}, \mathbf{y}, \omega)$
π_g^n, v_{gi}^n	=	periodic vector Green's function $(\mathbf{x}, \mathbf{y}, t-\tau)$
ρ_∞	=	ambient density
τ_s	=	turbulent time scale
ϕ	=	azimuthal angle of observer
Ω	=	specific dissipation rate
ω	=	angular frequency

Subscripts

s	=	shock-cell fluctuation
t	=	turbulent fluctuation

I. Introduction

BROADBAND shock-associated noise (BBSAN) is one component of jet noise from supersonic jets operating at offdesign conditions. In this paper a model is developed to predict BBSAN. This component dominates the radiated noise at large angles relative to the jet downstream axis, when the jet is operating offdesign. The method builds on the noise generation mechanisms that have been proposed in existing prediction methods, but the focus is on the development of a new BBSAN prediction scheme that is free of the limitations of previous models. Only the operating conditions of an offdesign supersonic jet and the nozzle geometry need to be specified to make a prediction. The long-term goal of the present approach is to make BBSAN predictions from nozzles that are not axisymmetric and include highly offdesign operating conditions and realistic

Presented as Paper 2009-3315 at the 15th AIAA/CEAS Aeroacoustics Conference, Miami, FL, 11–13 May 2009; received 19 March 2010; revision received 17 August 2010; accepted for publication 21 August 2010.

*Boeing/A. D. Welliver Professor, Department of Aerospace Engineering, 229 Hammond Building. Fellow AIAA.

†Research Aerospace Engineer, Aeroacoustics Branch, 2 North Dryden Street, Mail Stop 461. Member AIAA.

engine nozzle geometries. However, the results in the present paper are primarily for axisymmetric jets operating at a variety of nozzle total pressure ratios (NPR $= p_o/p_\infty$) and total temperature ratios (TTR $= T_o/T_\infty$); a rectangular-nozzle case is also included.

Current prediction methods for BBSAN are based primarily on empirical correlations of radiated noise and jet data. These methods are restricted to axisymmetric single-stream, dual-stream, or simple rectangular-jet nozzle geometries. These BBSAN models were developed mainly based on observations in unheated jets, though some corrections for the effect of jet heating have been introduced. BBSAN is still a very important component of noise in hot jets. In heated jets, the BBSAN and mixing noise are often of the same intensity, though they radiate in different directions. Mixing noise is dominant in the jet's downstream arc and BBSAN is dominant in the upstream arc. However, this is only the case for the peak noise levels. At low frequencies in particular, the jet mixing noise is dominant at all angles to the jet axis. As will be shown, this is because the BBSAN spectrum decays very rapidly at low frequencies.

Broadband shock-associated noise is present in supersonic jets operating at offdesign conditions. This can occur for either convergent or convergent–divergent nozzles. Under these conditions, the pressure at the jet exit differs from the ambient value. This imbalance generates a system of shocks and expansions in the jet plume. The interaction between the turbulence in the jet shear layer and this shock-cell structure is the source of shock-associated noise. Shock-associated noise is observed as a strong spectral peak, with additional peaks at lower intensities at higher frequencies, at relatively large angles to the jet downstream axis. The peak frequency is a simple function of the jet shock-cell spacing and the convection velocity of the jet shear-layer turbulence. The amplitude of BBSAN depends on the ratio of observer distance to the jet diameter, the polar and azimuthal observer angles, the geometry of the nozzle, the degree of offdesign operation, and, to a lesser degree, the stagnation temperature. The degree of offdesign operation (the offdesign parameter) dependence is quantified by the factor β:

$$\beta = \sqrt{|M_j^2 - M_d^2|} \tag{1}$$

where M_d is the design Mach number of the nozzle, and M_j is the fully expanded jet Mach number, which depends solely on the NPR:

$$M_j = \left[\frac{2}{\gamma - 1}(\mathrm{NPR}^{\frac{\gamma-1}{\gamma}} - 1)\right]^{1/2} \tag{2}$$

where γ is the ratio of specific heats.

The first prediction scheme for broadband shock-associated noise was developed by Harper-Bourne and Fisher [1]. Their methodology and the resulting prediction scheme exemplify an excellent coupling of experimental observations and theory. Their proposition was that BBSAN depends on the nearly coherent interaction between the turbulence in the jet shear layer and the jet's nearly periodic shock-cell structure. This can be modeled as a series of correlated point sources that radiate either constructively or destructively. Harper-Bourne and Fisher's prediction scheme depends on a knowledge of the rate of decay of the turbulence correlation between shocks, as well as the characteristic spectral shape of the radiated noise generated by each interaction. These were obtained using a least-squares procedure to match the model with experimental noise measurements. The nozzles considered in the experiments were convergent and operated at TTR $= 1.0$. The method has also been applied to heated jets successfully but predictions were not shown in the original paper. The method is used in the SAE ARP876 [2] prediction for single-stream shock-associated noise from convergent nozzles at supercritical conditions and is also included as a module in the current version of the Aircraft Noise Prediction Program (ANOPP) [3].

A second prediction method for shock-associated noise was developed by Tam [4]. The basic physical model was that described by Tam and Tanna [5]. Tam [4] argued that the shock-cell structure in the jet could be modeled, following the work of Pack [6], as a waveguide, where the waves are forced by the pressure imbalance at the jet exit and are confined by the jet shear layer. The simplest model that can be used for the jet is a vortex sheet. The effects of the slow divergence of the jet and the dissipative effects of the turbulence on the shock cells can also be included in the same general framework as shown by Tam et al. [7]. The large-scale turbulence in the jet shear layer is modeled as a random superposition of instability waves supported by the jet mean flow, as described by Tam and Chen [8]. The interaction between the downstream-traveling instability waves and the nearly periodic shock-cell structure results in an interference pattern of traveling waves. The phase velocity of these waves can be greater than that of the instability waves alone and gives rise to noise radiation at large angles to the jet downstream axis, including the upstream direction. Since there is a random set of instability waves interacting with the shock cells, the resulting radiation pattern involves broad lobes rather than a sharply directional radiation. Tam [4] argued that a complete calculation of the large-scale turbulence spectrum would be computationally very expensive. So the eventual prediction formula is based on a simple growth and decay formula for the instability waves and their phase velocity and on empirical formulas to correct the shock-cell spacing from the vortex sheet approximation. In addition, the spectral width is determined with a best fit to the measured noise data. The predictions give good overall agreement with noise measurements in both the jet's near and far fields and certain key features of the measured spectra are captured. These include the variation of the frequency of the broadband spectral peak with observer angle (the same prediction is provided by the Harper-Bourne and Fisher [1] model), the narrowing of the spectral shapes as the observer moves towards the jet upstream direction, and the presence of secondary spectral peaks at higher frequencies than the main peak. It should be noted that the Harper-Bourne and Fisher [1] model also predicted multiple harmonics of the shock peak with decreasing amplitude when the nonuniform spacing of the shock cells was included. Tam [9] extended his original model to account for jets operating at moderately offdesign conditions as well as to incorporate a correction for the effect of jet heating (though no comparisons were shown for heated cases). More recent versions of ANOPP [3] have incorporated Tam's [9] model for BBSAN.

Lele [10] compared the models of Harper-Bourne and Fisher [1] and Tam [9] and argued that a distributed phased-array of noise sources can be used to interpret Tam's model. Lele's [10] comparison of the two models showed that in some select cases a modified form of the model of Harper-Bourne and Fisher [1] compared more favorably than Tam's [9] with respect to experimental data. However, comparisons were only made for slightly offdesign jets and a small amount of heating.

Recently, numerical simulations of supersonic jets operating offdesign have been performed. Notable examples are the studies by Shur et al. [11,12], using a hybrid Reynolds-averaged Navier–Stokes (RANS) with large eddy simulation method. These studies included simulations of unheated and heated jets as well as jets operating at offdesign conditions. Nonsimple geometries, including a beveled nozzle and simulated chevrons were studied. The results are very encouraging and indicate the quality of noise predictions that can be achieved through a judicious use of discretization method, grid distribution, and turbulence modeling. However, the computations are still expensive and time-consuming.

In the present approach, the development of the jet flow, including the internal flow in the nozzle, is predicted using a steady RANS calculation. A two-equation turbulence model is used. These calculations are much faster than time-accurate flow simulations. The results of the RANS simulations are used to characterize the jet mean flow, including the jet's shock-cell structure, as well as to provide estimates of the turbulent fluctuation levels and the turbulent length and time scales. The incorporation of this information within the BBSAN noise model described below enables the BBSAN to be predicted on the basis of the jet nozzle geometry and operating conditions alone.

In the next section the BBSAN prediction formulas are developed. The flow simulations and their validation are then described, as is the numerical implementation of the model. Predictions are then performed for single axisymmetric jets operating at under- and

overexpanded conditions. The effects of jet heating are also demonstrated. Comparisons are made with both measurements and existing BBSAN noise prediction models. An example of the use of the model for a rectangular-jet case is also included. The effect of the choice of calibration case for the model's empirical coefficients is described in Appendix A.

II. Broadband Shock-Associated Noise Model Development

The BBSAN model builds on the analysis developed by Tam [4]. Tam's analysis is considerably simplified if the following forms of the inviscid compressible equations of motion are used:

$$\frac{D\pi}{Dt} + \frac{\partial v_i}{\partial x_i} = 0 \tag{3}$$

$$\frac{Dv_i}{Dt} + a^2 \frac{\partial \pi}{\partial x_i} = 0 \tag{4}$$

$$\frac{D}{Dt} = \frac{\partial}{\partial t} + v_i \frac{\partial}{\partial x_i} \tag{5}$$

where a is the local speed of sound, v_i are the velocity components in the x_i directions of a Cartesian coordinate system, and π is related to the logarithm of the pressure p:

$$\pi = \frac{1}{\gamma} \ell_n (p/p_\infty) \tag{6}$$

Following Tam [4], the instantaneous flowfield properties are separated into four components; that is,

$$\begin{bmatrix} \pi \\ v_i \end{bmatrix} = \begin{bmatrix} \bar{\pi} + \pi_s + \pi_t + \pi' \\ \bar{v}_i + v_{si} + v_{ti} + v_i' \end{bmatrix} \tag{7}$$

where the overbar denotes the long-time-averaged value, the subscript s denotes the perturbations associated with the shock-cell structure, the subscript t denotes the fluctuations associated with the turbulence, and the prime denotes the fluctuations generated by the interaction of the turbulence and the shock-cell structure. It will be assumed that the shock-cell structure satisfies the steady linearized version of Eqs. (3) and (4). In addition, it is assumed that the unsteady linearized version of these equations is also satisfied by the turbulent velocity fluctuations. This is justified if the important components of the turbulence, as far as the broadband shock-associated noise is concerned, are coherent over relatively large axial distances. These components are described well by a linear instability wave model.

On making these assumptions, the inhomogeneous equations for the fluctuations associated with the interaction of the turbulence with the shock cells can be written:

$$\frac{\partial \pi'}{\partial t} + \bar{v}_j \frac{\partial \pi'}{\partial x_j} + \frac{\partial v_i'}{\partial x_i} = \theta \tag{8}$$

$$\frac{\partial v_i'}{\partial t} + \bar{v}_j \frac{\partial v_i'}{\partial x_j} + v_j' \frac{\partial \bar{v}_i}{\partial x_j} + \bar{a}^2 \frac{\partial \pi'}{\partial x_i} = f_i^v + f_i^a \tag{9}$$

The terms on the left-hand sides of Eqs. (8) and (9) are the linearized Euler equations in terms of the perturbation quantities π' and v_i'. The terms that appear on the right-hand sides represent the sources of the BBSAN. They are defined by

$$\theta = -v_{sj} \frac{\partial \pi_t}{\partial x_j} - v_{tj} \frac{\partial \pi_s}{\partial x_j} \tag{10}$$

$$f_i^v = -v_{sj} \frac{\partial v_{ti}}{\partial x_j} - v_{tj} \frac{\partial v_{si}}{\partial x_j} \tag{11}$$

and,

$$f_i^a = -a_s^2 \frac{\partial \pi_t}{\partial x_i} - a_t^2 \frac{\partial \pi_s}{\partial x_i} \tag{12}$$

where θ is a dilatation rate generated by the interaction between the shock cell and turbulent pressure gradients and velocity perturbations, f_i^v is the unsteady force per unit volume associated with interactions between the turbulent velocity fluctuations and the velocity perturbations associated with the shock cells, and f_i^a is the unsteady force per unit volume related to the interaction of fluctuations in the sound speed (or temperature), caused by the turbulence and the shock cells, and the associated pressure gradients. In traditional approaches to turbulence mixing noise, these equivalent sources have been treated separately and, for the moment, the same assumption will be made here. The solution to Eqs. (8) and (9) can be written in terms of the vector Green's function that satisfies the equations

$$\frac{\partial \pi_g^n}{\partial t} + \bar{v}_j \frac{\partial \pi_g^n}{\partial x_j} + \frac{\partial v_{gi}^n}{\partial x_i} = \delta(\mathbf{x} - \mathbf{y}) \delta(t - \tau) \delta_{0n} \tag{13}$$

$$\frac{\partial v_{gi}^n}{\partial t} + \bar{v}_j \frac{\partial v_{gi}^n}{\partial x_j} + v_{gj}^n \frac{\partial \bar{v}_i}{\partial x_j} + \bar{a}^2 \frac{\partial \pi_g^n}{\partial x_i} = \delta(\mathbf{x} - \mathbf{y}) \delta(t - \tau) \delta_{\text{in}} \tag{14}$$

where $\pi_g^n = \pi_g^n(\mathbf{x}, \mathbf{y}, t - \tau)$ and $v_{gi}^n = v_{gi}^n(\mathbf{x}, \mathbf{y}, t - \tau)$ are the components of the vector Green's function, $\mathbf{x}$ denotes the observer position, $\mathbf{y}$ denotes the source location, $\delta()$ is the Dirac delta function, δ_{ij} is the Kronecker delta function, and τ is the source emission time. For small perturbation pressures, $\pi' \simeq p'/(\gamma p_\infty) = p'/(\rho_\infty a_\infty^2)$. Then the solution for the far-field pressure $p'(\mathbf{x}, t)$ can be written

$$p'(\mathbf{x}, t) = \rho_\infty a_\infty^2 \int_{-\infty}^{\infty} \cdots \int_{-\infty}^{\infty} \left\{ \pi_g^0(\mathbf{x}, \mathbf{y}, t - \tau) \theta(\mathbf{y}, \tau) + \sum_{n=1}^{3} \pi_g^n(\mathbf{x}, \mathbf{y}, t - \tau) [f_n^v + f_n^a](\mathbf{y}, \tau) \right\} \mathrm{d}\tau \, \mathrm{d}\mathbf{y} \tag{15}$$

The periodic Green's function is also introduced, given by

$$\pi_g^n(\mathbf{x}, \mathbf{y}, t - \tau) = \frac{1}{2\pi} \int_{-\infty}^{\infty} \pi_g^n(\mathbf{x}, \mathbf{y}, \omega) \exp[-i\omega(t - \tau)] \, \mathrm{d}\omega \tag{16}$$

$$\pi_g^n(\mathbf{x}, \mathbf{y}, \omega) = \int_{-\infty}^{\infty} \pi_g^n(\mathbf{x}, \mathbf{y}, t - \tau) \exp[i\omega(t - \tau)] \, \mathrm{d}t \tag{17}$$

From this point, only the source term associated with the velocity perturbations will be considered. It is expected that the scaling of the other source terms would be similar. The exception would be the source term associated with the temperature fluctuations. However, the importance of this term remains the subject of debate in the prediction of turbulent mixing noise in heated jets. The simulations by Ray [13] suggest that this entropic term is not important in unheated jets. So, for the moment, this term will not be considered further. Then the pressure is given by

$$p'(\mathbf{x}, t) = \frac{\rho_\infty a_\infty^2}{2\pi} \int_{-\infty}^{\infty} \cdots \int_{-\infty}^{\infty} \pi_g^n(\mathbf{x}, \mathbf{y}, \omega) f_n^v(\mathbf{y}, \tau) \times \exp[-i\omega(t - \tau)] \, \mathrm{d}\omega \, \mathrm{d}\tau \, \mathrm{d}\mathbf{y} \tag{18}$$

Now the autocorrelation of the pressure can be formed. It is given by

$$\overline{p'(\mathbf{x}, t) p'(\mathbf{x}, t + \tau^*)} = \frac{\rho_\infty^2 a_\infty^4}{(2\pi)^2} \int_{-\infty}^{\infty} \cdots \int_{-\infty}^{\infty} \sum_{n=1}^{3} \sum_{m=1}^{3} \pi_g^n(\mathbf{x}, \mathbf{y}, \omega_1) \pi_g^m(\mathbf{x}, \mathbf{z}, \omega_2) \times \overline{f_n^v(\mathbf{y}, \tau_1) f_m^v(\mathbf{z}, \tau_2)} \exp[-i\omega_1(t - \tau_1) - i\omega_2(t - \tau_2) - i\omega\tau^*] \, \mathrm{d}\omega_1 \, \mathrm{d}\omega_2 \, \mathrm{d}\tau_1 \, \mathrm{d}\tau_2 \, \mathrm{d}\mathbf{y} \, \mathrm{d}\mathbf{z} \tag{19}$$

The spectral density is given by the Fourier transform of the autocorrelation of the pressure:

$$S(\mathbf{x},\omega)=\int_{-\infty}^{\infty}\overline{p'(\mathbf{x},t)p'(\mathbf{x},t+\tau^*)}\exp(i\omega\tau^*)\,\mathrm{d}\tau^* \tag{20}$$

The integration with respect to τ^* can be performed immediately.

Before proceeding it is necessary to examine the form of the two-point cross-correlation of f_n^v. It is dependent on the strength of the shock cells and the turbulent fluctuations and its product is significant in regions where the shocks and expansions intersect with the turbulent shear layer. It is assumed that the two-point cross-correlation function of the BBSAN source term can be written as

$$\overline{f_n^v(\mathbf{y},\tau_1)f_m^v(\mathbf{z},\tau_2)}=R_{nm}^v(\mathbf{y},\boldsymbol{\eta},\tau) \tag{21}$$

where $\boldsymbol{\eta}=\mathbf{z}-\mathbf{y}$ and $\tau=\tau_2-\tau_1$. This is consistent with the statistics of the turbulence being locally a function of the separation distance and time delay between the two source locations. Then the integrations with respect to τ_1, ω_1, and ω_2 can be performed, giving

$$\begin{aligned}S(\mathbf{x},\omega)=\rho_\infty^2a_\infty^4\int_{-\infty}^{\infty}\cdots\int_{-\infty}^{\infty}\sum_{n=1}^{3}\sum_{m=1}^{3}\pi_g^n(\mathbf{x},\mathbf{y},-\omega)\\ \times\pi_g^m(\mathbf{x},\mathbf{y}+\boldsymbol{\eta},\omega)R_{nm}^v(\mathbf{y},\boldsymbol{\eta},\tau)\exp(i\omega\tau)\,\mathrm{d}\tau\,\mathrm{d}\boldsymbol{\eta}\,\mathrm{d}\mathbf{y}\end{aligned} \tag{22}$$

The Green functions could be calculated numerically for a given mean flow. This could involve a locally parallel approximation or the full diverging flow. The problem could also be formulated in terms of the adjoint Green's function for the linearized Euler equations, as described by Tam and Auriault [14]. This approach is presently being taken by the authors, as it appears to be important for dual-stream jets. However, BBSAN is radiated predominantly at large angles to the jet downstream axis, where the refractive effects of the mean flow would be small or absent. In view of this, the Green function is approximated by the Green function in the absence of a mean flow. The components of the vector Green's function are then readily related to the Green function of the Helmholtz equation. In the far field, for $|\mathbf{y}|\ll|\mathbf{x}|$,

$$\pi_g^n(\mathbf{x},\mathbf{y},\omega)=-\frac{i\omega}{4\pi a_\infty^3R}\frac{x_n}{R}\exp\left[\frac{i\omega|\mathbf{x}-\mathbf{y}|}{a_\infty}\right] \tag{23}$$

where x_n is the nth component of $\mathbf{x}$, and R is the magnitude of $\mathbf{x}$. Then,

$$\pi_g^m(\mathbf{x},\mathbf{y}+\boldsymbol{\eta},\omega)=\pi_g^m(\mathbf{x},\mathbf{y},\omega)\exp\left\{-i\frac{\omega\mathbf{x}}{a_\infty R}\cdot\boldsymbol{\eta}\right\} \tag{24}$$

With the use of these approximate forms for the far-field Green's functions, the spectral density can be written as

$$\begin{aligned}S(\mathbf{x},\omega)=\frac{\rho_\infty^2\omega^2}{16\pi^2a_\infty^2R^2}\int_{-\infty}^{\infty}\cdots\int_{-\infty}^{\infty}\frac{x_nx_m}{R^2}R_{nm}^v(\mathbf{y},\boldsymbol{\eta},\tau)\\ \times\exp\left[i\omega\left(\tau-\frac{\mathbf{x}\cdot\boldsymbol{\eta}}{Ra_\infty}\right)\right]\mathrm{d}\tau\,\mathrm{d}\boldsymbol{\eta}\,\mathrm{d}\mathbf{y}\end{aligned} \tag{25}$$

The summation terms in Eq. (25) are not shown but are implied by the repeated subscripts n and m.

From the form of f_i^v given by Eq. (11), and on dimensional grounds, it is taken to scale as

$$f_i^v\sim\frac{p_sv_t}{\rho_\infty a_\infty l} \tag{26}$$

where p_s represents the shock-cell strength, v_t is a characteristic turbulent velocity fluctuation, and l is a characteristic turbulent length scale. These will be determined from the RANS computational fluid dynamics (CFD) solution. For simplicity, use is also made of the Proudman form for the cross-correlation; that is,

$$\frac{x_nx_m}{R^2}R_{nm}^v(\mathbf{y},\boldsymbol{\eta},\tau)=R_{xx}^v(\mathbf{y},\boldsymbol{\eta},\tau) \tag{27}$$

where $R_{xx}^v(\mathbf{y},\boldsymbol{\eta},\tau)=\langle f_x^v(\mathbf{y},t)f_x^v(\mathbf{y}+\boldsymbol{\eta},t+\tau)\rangle$, and f_x^v is the component of f_i^v in the direction of the observer.[‡] Use of these relationships gives

$$R_{xx}^v(\mathbf{y},\boldsymbol{\eta},\tau)=\frac{1}{\rho_\infty^2a_\infty^2l^2}p_s(\mathbf{y})p_s(\mathbf{y}+\boldsymbol{\eta})R^v(\mathbf{y},\boldsymbol{\eta},\tau) \tag{28}$$

where

$$R^v(\mathbf{y},\boldsymbol{\eta},\tau)=\overline{v_x(\mathbf{y},t)v_x(\mathbf{y}+\boldsymbol{\eta},t+\tau)} \tag{29}$$

is the two-point cross-correlation function of the turbulent velocity fluctuations in the observer direction.

The far-field spectral density can then be written as

$$\begin{aligned}S(\mathbf{x},\omega)=\frac{\omega^2}{16\pi^2a_\infty^4R^2}\int_{-\infty}^{\infty}\cdots\int_{-\infty}^{\infty}\frac{1}{l^2}p_s(\mathbf{y})p_s(\mathbf{y}+\boldsymbol{\eta})R^v(\mathbf{y},\boldsymbol{\eta},\tau)\\ \times\exp\left[i\omega\left(\tau-\frac{\mathbf{x}\cdot\boldsymbol{\eta}}{Ra_\infty}\right)\right]\mathrm{d}\tau\,\mathrm{d}\eta\,\mathrm{d}\mathbf{y}\end{aligned} \tag{30}$$

It is convenient to introduce the cross spectral density of the turbulent velocity fluctuations. This enables the turbulent velocity statistics to be characterized either in terms of the cross-correlation or cross spectral density. The cross spectral density is given by

$$S^v(\mathbf{y},\boldsymbol{\eta},\omega)=\int_{-\infty}^{\infty}R^v(\mathbf{y},\boldsymbol{\eta},\tau)\exp(i\omega\tau)\,\mathrm{d}\tau \tag{31}$$

To emphasize the quasi-periodic nature of the shock-cell structure and to assist in the implementation of the model, the axial spatial Fourier transform of the shock cell's pressure perturbation is defined. It is given by

$$\begin{aligned}p_s(\mathbf{y})&=\frac{1}{2\pi}\int_{-\infty}^{\infty}\tilde{p}_s(k_1,y_2,y_3)\exp[ik_1y_1]\,\mathrm{d}k_1\\ \tilde{p}_s(k_1,y_2,y_3)&=\int_{-\infty}^{\infty}\tilde{p}_s(\mathbf{y})\exp[-ik_1y_1]\,\mathrm{d}y_1\end{aligned} \tag{32}$$

where k_1 is the wave number in the axial y_1 direction. These relationships can be substituted into Eq. (30). It should be noted that the axial Fourier transform of the shock-cell pressure perturbation is only applied to one of the two terms in the integrand. This has been found to be convenient in the evaluation of the BBSAN noise prediction formula given below. After some integrations, the spectral density is found to be given by

$$\begin{aligned}S(\mathbf{x},\omega)=\frac{\omega^2}{32\pi^3a_\infty^4R^2}\int_{-\infty}^{\infty}\cdots\int_{-\infty}^{\infty}\frac{1}{l^2}p_s(\mathbf{y})\tilde{p}_s(k_1,y_2+\eta,y_3+\zeta)\\ \times\exp[ik_1(y_1+\xi)]S^v(\mathbf{y},\boldsymbol{\eta},\omega)\exp\left[-i\omega\frac{\mathbf{x}\cdot\boldsymbol{\eta}}{Ra_\infty}\right]\mathrm{d}k_1\,\mathrm{d}\boldsymbol{\eta}\,\mathrm{d}\mathbf{y}\end{aligned} \tag{33}$$

with $\boldsymbol{\eta}=(\xi,\eta,\zeta)$.

A model is now proposed for $R^v(\mathbf{y},\boldsymbol{\eta},\tau)$ in the form

$$\begin{aligned}R^v(\mathbf{y},\boldsymbol{\eta},\tau)=K\exp[-|\tau|/\tau_s]\exp[-(\xi-\bar{u}_c\tau)^2/l^2]\\ \times\exp[-(\eta^2+\zeta^2)/l_\perp^2]\end{aligned} \tag{34}$$

where τ_s is the turbulent time scale, $l_\perp$ is the turbulent length scale in the cross-stream direction, and K is the turbulent kinetic energy. The scales τ_s, l, and $l_\perp$ are found directly from the CFD RANS solution. It should be noted that this form has been chosen, to some extent, for being a reasonable representation as well as being convenient. However, it clearly denies the possibility of there being significant

[‡]It should be noted that these simplifications could be relaxed and a more complicated anisotropic model could be used for the turbulence statistics. However, in the early development of the model described here, the simplest modeling assumptions have been made.

negative loops in the cross-correlation. The effect of this omission and the use of the simplified form of cross-correlation given by Eq. (34) is being considered by the authors.

The observer location is now written in spherical polar coordinates, given by

$$\mathbf{x} = R(\cos\theta, \sin\theta\cos\varphi, \sin\theta\sin\varphi) \tag{35}$$

Then the far-field spectral density can be written as

$$S(\mathbf{x},\omega) = \frac{1}{16\pi\sqrt{\pi}a_\infty^4 R^2}\int_{-\infty}^{\infty}\cdots\int_{-\infty}^{\infty}\left\{\frac{Kl_\perp^2}{l\tau_s}p_s(\mathbf{y})\tilde{p}_s(k_1,y_2,y_3)\exp(ik_1y_1) \times\frac{\omega^2\tau_s^2\exp[-l^2(k_1-\omega\cos\theta/a_\infty)^2/4-\omega^2l_\perp^2\sin^2\theta/4a_\infty^2]}{[1+(1-M_c\cos\theta+\bar{u}_ck_1/\omega)^2\omega^2\tau_s^2]}\right\}\mathrm{d}k_1\,\mathrm{d}\mathbf{y} \tag{36}$$

In the derivation of Eq. (36) it has been assumed that the shock-cell structure is independent of the cross-stream direction over the distance of significant cross-correlation of the velocity fluctuations, such that $\tilde{p}_s(k_1, y_2+\eta, y_3+\zeta)$ can be replaced by $\tilde{p}_s(k_1, y_2, y_3)$.

Equation (36) provides the prediction formula for the BBSAN. All of the parameters can be determined from a RANS CFD solution. In the case of an axisymmetric jet, the integrations with respect to the cross-stream direction can be reduced to a single integration in the radial direction. The implementation of this prediction model is described in the next section.

III. Implementation

The implementation of the BBSAN model developed in the previous section requires a RANS solution from a CFD solver using a two-equation turbulence model. The NPARC Alliance Wind-US [15] CFD solver has been used to generate the RANS solutions. Computational grids for the RANS solver are constructed with Gridgen using the exact dimensions of the nozzles of the corresponding experiments. Nozzle coordinates are loaded as databases in Gridgen and the nozzle contour is formed from them. The inlet of the nozzle is extended upstream for stability purposes, but this does not affect the flowfield in the jet itself. If the lip thickness of the nozzle is known, then its value is also used. Otherwise the nozzle lip thickness is set to zero. All the nozzles used in the present paper use accurate nozzle lip thicknesses. The computational grids are all structured for finite difference schemes. However, unstructured finite element computational grids could also be used. The prediction scheme itself is independent of the type of computational grid. Boundary conditions for the RANS calculations include an inlet boundary condition for the nozzle inflow, freestream boundary conditions for the far field, a downstream pressure condition for the jet outflow, an axisymmetric boundary condition along the jet centerline, and no-slip walls. Slip walls are specified on the inside of the nozzle wall near the inlet boundary, but these transition into no-slip walls upstream of the converging section of the nozzle. The boundary conditions in the far field are specified by setting an ambient pressure, temperature, and a freestream velocity of $0.001c_\infty$ for stability. The inlet boundary conditions control the physics of the jet by holding the total pressure and total temperature to values based on the experimental NPR and TTR. An initial inflow Mach number is also set, but it is allowed to vary, whereas the total values remain constant. The computational domain extends 75 nozzle diameters downstream from the nozzle exit plane and 50 diameters in the cross-stream direction. The RANS solutions are based on the Menter [16] shear stress transport (SST) turbulence model that provides the mean quantities, including K and Ω, where K is the turbulent kinetic energy per unit volume and Ω is the specific dissipation rate. The number of grid points in a typical calculation for an axisymmetric jet is 200,000 to 500,000. Solutions of the flowfield are overresolved and a much lower number of grid points in the computational domain could be used. The flows have been overresolved so that grid independence studies of the various BBSAN calculations could be performed by interpolating to lower resolutions. Grid convergence studies were performed in Wind-US using grid sequencing. The RANS CFD simulations have been validated by comparisons with experimental measurements in shock-containing jets. This is described by Miller et al. [17].

The integration in Eq. (36) is performed on a structured grid with constant spacing between grid points. This is done for two reasons. First, this method allows grid independence studies using the highly resolved CFD solution databases. Second, it simplifies the calculation of the Fourier transform of p_s, since the grid spacing is constant with respect to x, r or y, and z. Thus, a standard discrete Fourier transform or fast Fourier transform library can be used. This also ensures that the radial locations of $\tilde{p}_s$ and the other field variables are the same. Arrays that hold interpolated values in the integration regions are allocated based on the values in the parameter input file. Interpolation of CFD data is performed with an inverse weighted interpolation scheme. Two interpolated regions are constructed. The first is the source integration region and consists of a structured computational grid in two- or three dimensions over the sources of the BBSAN. The second interpolated region is the wave-number integration region, which also has constant grid-point spacing. The range of the wave-number integration region in the axial direction is based on the desired axial wave-number resolution.

The variables that are interpolated onto the integration region are K, ε, p, and u. Figure 1 shows the integration region superimposed on the CFD solution with contours of u for the axisymmetric jet with $M_d = 1.00$, $M_j = 1.50$, TTR $= 1.00$, and $D = 0.0127$ m. The CFD solution is axisymmetric and is only calculated for the top half plane.

The characteristic scales required in the BBSAN model are found from K and ϵ on the interpolated integration region. The time and length scales are taken to be $\tau_s = c_\tau K/\epsilon$, $l = c_l K^{3/2}/\epsilon$, and $l_\perp = c_\perp l$, where c_τ, c_l, and $c_\perp$ are constants. These three constants are the same for all jet conditions. An additional constant, P_f, is needed in the model to scale the amplitude of the spectral density. The scaling is the same for all jet operating conditions and a good value is $P_f = 10^{1.2} = 15.85$. The constants used in all the predictions shown below are $c_\tau = 1.25$, $c_l = 3.25$, and $c_\perp = 0.30$. These constants are found by performing a parametric study relative to a single selected jet condition and observer angle with various sets of experimental

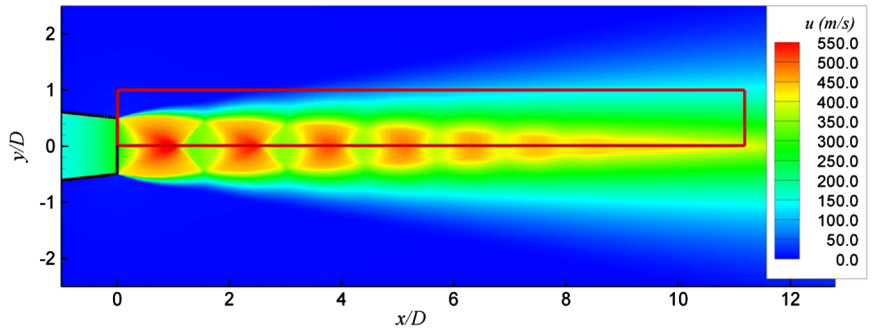

Fig. 1 Interpolation of u m/s onto the integration region from the CFD solution, for $M_d = 1.00$, $M_j = 1.50$, TTR $= 1.00$, and $D_j = 0.0127$ m. The line encloses the source integration region.

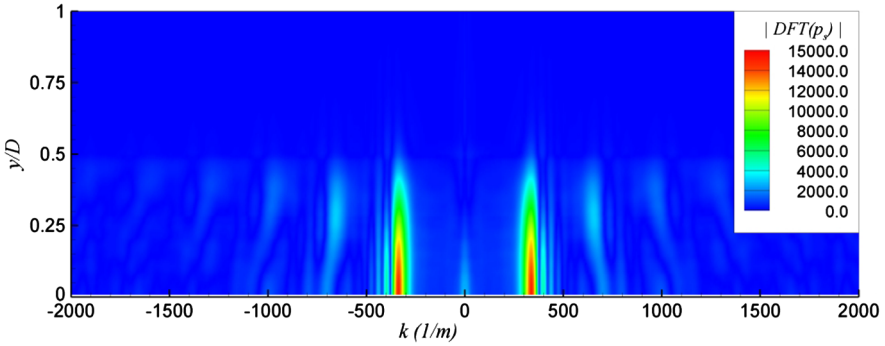

Fig. 2 Magnitude of the Fourier transform of the shock-cell pressure, $|\tilde{p}_s|$.

data. The results presented below use the same coefficients for all the predictions.

Once the field variables have been interpolated onto the source and wave-number integration regions, the shock-cell pressure is found by subtracting the ambient pressure. Note that the integration region is only downstream of the nozzle exit. The shock pressure is mirrored across $x/D = 0$, so that the discrete data of p_s form an even function and a discrete Fourier transform results in a real result. The Fourier transform of the shock pressure is taken with respect to the streamwise direction, x after a Hanning window has been applied. Values of $\tilde{p}_s$ are real and the magnitude of the shock pressure, $|\tilde{p}_s|$, is shown in Fig. 2. It is shown below that each of the peaks of the wave-number spectrum, $\tilde{p}_s$, contributes to peaks in the predicted BBSAN spectrum. The strongest peak in the spectrum corresponds to the fundamental shock-cell spacing and the subsequent peaks at higher wave number correspond to its spatial harmonics. The waveguide model for the shock-cell structure given by Pack [6] would give only lines in the spectrum.

Before describing the BBSAN noise predictions, the effect of temperature on the radiated noise should be considered. It is clear from Eq. (36) that the source strength is controlled by the shock-cell strength and the turbulent kinetic energy. The former would be expected to be unaffected by heating at a fixed pressure ratio, but the latter will depend approximately on the square of the jet exit velocity. Thus, as the jet heating is increased, the level of BBSAN should also increase. This was not noted in the paper of Harper-Bourne and Fisher [1], but they report good agreement in predictions for jets operating at 1100 K. Recently, a large number of measurements have been carried out by Viswanathan et al. [18] that confirm the scaling of BBSAN with TTR. Although heating initially increases the BBSAN levels, the levels remain almost unchanged with further increases in total temperature. The reason for this is unclear but intriguing. Tam [9] introduced a temperature correction effect in his BBSAN model and the same correction is used here. That is, the spectral densities are multiplied by a temperature correction factor:

$$T_{\mathrm{cf}} = \frac{\rho_j}{\rho_\infty}\left(1 + \frac{\gamma - 1}{2} M_j^2\right)^{-1} \tag{37}$$

It should be noted that this has a smooth variation with temperature increase, not the steplike character observed in the measurements.

IV. Results

The scaling coefficients in the BBSAN model control the shape of the spectrum and, in part, its magnitude. c_τ is set to 1.25 and controls the relative magnitude of the spectrum and is the primary means to control the sharpness of each BBSAN peak. c_l is set to 3.25 and determines the turbulent length scale in the streamwise direction. It controls to some degree the width of the peaks, the smoothness of the spectra, and the relative magnitude of the BBSAN as a function of observer angle. Increasing c_l smooths the BBSAN peaks, increases the width of each peak in the BBSAN spectrum, and lowers the relative magnitude between the peaks and troughs. It should be noted that the value of c_l of 3.25 is much larger than that used by Tam and Auriault [14] in their model of fine-scale turbulent mixing noise. This reflects the fact that BBSAN is controlled by the large-scale structures in the jet shear layer that are coherent over relatively large axial distances. The coefficient $c_\perp$ is set according to experimental observations, which show that the cross-stream length scale is approximately 30% of the streamwise length scale and is therefore set to 0.30. The value of $c_\perp$ controls the rate at which the high-frequency predictions decay. These values were chosen based on the predicted spectrum of a jet at $\theta = 100°$, operating at $M_d = 1.00$, $M_j = 1.50$, and TTR = 1.00. Finally, P_f is chosen by matching the BBSAN peaks at $\theta = 100°$. The same values of c_τ, c_l, $c_\perp$, and P_f are used for all the calculated spectral density shown below.

A. Single-Stream Axisymmetric Jets

BBSAN predictions have been made for the jet conditions shown in Table 1 based on corresponding Wind-US CFD solutions using the Menter [16] SST turbulence model. The cases selected include both unheated and heated jets operating at over- and underexpanded conditions for two different nozzle geometries with design Mach numbers $M_d = 1.00$ (convergent) and $M_d = 1.50$ (convergent–divergent). Only selected cases are shown in this section. The CFD simulations for all the cases use a jet exit diameter, $D = 0.0127$ m.

Table 1 Jet operating conditions for the RANS CFD and BBSAN predictions

M_d	M_j	NPR	TTR	D, m	D_j, m	f_c	β	T_j, K	U_j, m/s
1.00	1.22	2.50	1.00	0.0508	0.0517	7,116	0.704	225.6	368.3
1.00	1.22	2.50	2.20	0.0508	0.0517	10,554	0.704	496.1	546.2
1.00	1.22	2.50	3.20	0.0508	0.0517	12,729	0.704	721.6	658.7
1.00	1.47	3.50	3.20	0.0508	0.0546	13,792	1.073	655.5	752.8
1.00	1.64	4.50	3.20	0.0508	0.0575	14,102	1.298	610.1	811.2
1.00	1.50	3.67	1.00	0.0127	0.0138	31,031	1.118	202.1	427.4
1.00	1.50	3.67	2.20	0.0127	0.0138	46,026	1.118	444.6	633.9
1.50	1.30	2.77	1.00	0.0127	0.0121	31,887	0.749	219.0	385.6
1.50	1.30	2.77	2.20	0.0127	0.0121	47,296	0.749	481.8	571.9
1.50	1.40	3.18	1.00	0.0127	0.0124	32,923	0.540	210.5	407.0
1.50	1.60	4.25	1.00	0.0127	0.0131	34,097	0.557	193.8	446.4
1.50	1.70	4.94	1.00	0.0127	0.0135	34,285	0.801	185.6	464.4
1.50	1.70	4.94	2.20	0.0127	0.0135	50,853	0.801	408.4	688.9

However, other CFD simulations for the same operating conditions but with different diameters have been performed and the results are very similar for the BBSAN prediction.

The BBSAN predictions are made at various angles θ from the downstream jet axis at a radial polar distance of 100 D from the center of the jet exit. Predictions are lossless and the corresponding experimental data in each case have been corrected for humidity and atmospheric absorption, so that the presented sound pressure levels (SPLs) are also lossless. The experimental data provided by Boeing was measured at 97.5 D from the nozzle exit, and the Pennsylvania State University (PSU) data was measured at 150 D. Both sets of data have been corrected to 100 D. The PSU experimental data have the origin for the observer position in spherical coordinates centered at $x/D = 5.0$ or 0.0635 m, but this is of less importance for BBSAN, since the source region is relatively close to the jet exit and the dominant radiation is at large angles to the jet downstream axis. The Boeing experiments were performed with heated air, and the PSU experiments were performed with helium/air mixtures to simulate heated jets. The exit diameter of the convergent nozzle in the Boeing experiments is 0.0622 m (2.45 in.), and the diameter of the PSU nozzle is 0.0127 m (1/2 in.). Experimental data, measured in the Small Hot Jet Acoustic Rig (SHJAR) facility at the NASA John H. Glenn Research Center at Lewis Field, have also been used for evaluation of the predictions. The SHJAR jet nozzle has a 2 in. diameter with microphones at $R/D = 50$ with an origin at the center of the nozzle exit. These data have also been scaled to 100 D.

The source integration regions chosen for the convergent jets with $D = 0.0127$ m are $0.0001 \leq x \leq 0.1421$ m and $0.0001 \leq r \leq 0.0127$ m with 300 and 75 grid points in the x and r directions, respectively. The shock pressure used for the Fourier transform was taken from $0.0001 \leq x \leq 0.4000$ m using 512 grid points. The data are mirrored about $x/D = 0.0$, so the total number of points in the Fourier transform is 1024. This yields a wave-number spacing Δk of approximately 7.86 m^{-1}. The source integration region for the convergent–divergent jets is $0.0001 \leq x \leq 0.1421$ m and $0.0001 \leq r \leq 0.0127$ m with 400 and 100 grid points in the x and y directions, respectively, while the wave-number integration range remains the same.

The model developed in the present paper is only for the BBSAN, which is only one of the components of offdesign supersonic jet noise. Thus, it is useful to separate the individual noise components from the total spectrum. Viswanathan [19] has developed a framework that separates the individual components of the total noise spectra into mixing noise and BBSAN. The Boeing data presented below for the converging nozzle predictions show this breakdown to help illustrate the capability of the prediction scheme. Specifically, the proposed model for BBSAN is compared directly against the extracted shock component from the total noise for the two convergent nozzle cases.

The BBSAN predictions are presented in terms of SPL per unit Strouhal number St. The case that has been used to fix the coefficients for the turbulence scales is the underexpanded converging jet with $M_j = 1.50$ and TTR = 1.00. Results of the model prediction in this case, in addition to various experiments, are shown in Fig. 3. There are eight comparisons of the predictions with experimental data for different observer angles θ with respect to the downstream jet axis. Each comparison is labeled with its corresponding observer angle and the maximum SPL level of the experiments conducted by Boeing. The screech tones are not used to find the maximum value. Experimental data from Boeing, NASA, and PSU are shown for each observer angle. Though there are minor differences between the different sets of experimental data, the overall agreement is good. Also shown are predictions based on the BBSAN prediction formulas provided by Tam [4,9] where appropriate. The breakdown of the total Boeing spectra into the BBSAN and mixing noise components is also shown. At the different observer angles the predictions are in good agreement with respect to all the experiments. The predictions capture the multiple peaks in the BBSAN spectra as well as the broadening in the spectral shape with decreasing angle to the jet downstream axis. For these operating conditions the amplitude of the primary peak in the BBSAN is relatively insensitive to the observer angle. This is captured by the predictions. It is important to emphasize that the predictions at every angle use the same scaling coefficients. As the angle to the jet downstream axis decreases, the primary peak in the BBSAN spectrum moves to higher Strouhal numbers. This is also predicted in the BBSAN models of Harper-Bourne and Fisher [1] and Tam [4]. The increase in the relative importance of the mixing noise at lower Strouhal numbers is evident in the experiments. Though this case was originally chosen to calibrate the model, the presence of screech tones makes this case not the best choice. In particular, it is known that the presence of screech can increase the turbulence levels and this is clear in measurements of the mixing noise component (see Viswanathan et al. [18]). An initial recalibration of the coefficients in a nonscreeching jet is given in Appendix A.

Before showing predictions for other jet operating conditions, it is interesting to show how the overall BBSAN is constructed. The

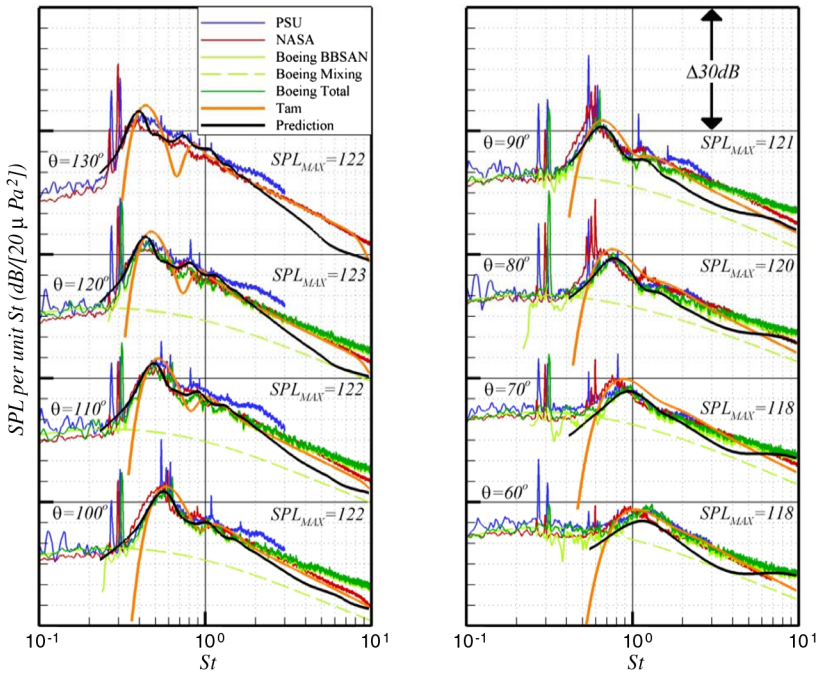

Fig. 3 Comparisons of BBSAN predictions with experiments for $M_d = 1.00$, $M_j = 1.50$, TTR = 1.00, and $R/D = 100$.

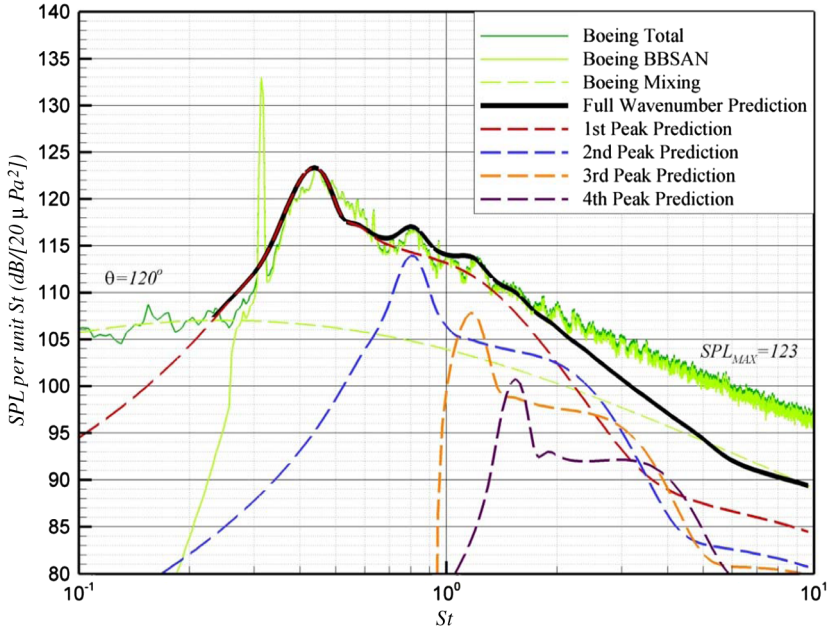

Fig. 4 Total BBSAN prediction and the accompanying contributions from selective integrations over contributing wave numbers of $\tilde{p}_s$ representing different waveguide modes of the shock-cell structure; $M_d = 1.00$, $M_j = 1.50$, TTR $= 1.00$, $R/D = 100$, and $\theta = 120.0$.

wave-number integration in Eq. (36) can be limited to contributions associated with individual components of the shock cell's wave-number spectrum. This is equivalent to examining the contributions of the interactions of the turbulence with the Fourier modes in a waveguide model of the shock-cell structure. Figure 4 shows these contributions and the corresponding peaks that they generate in the BBSAN spectrum. This selection of wave-number ranges replaces the summation over Fourier components of the waveguide model for the shock-cell structure in Tam's model [4]. However, in the present model, the spectral width is controlled by both the spectrum shape associated with the turbulent velocity fluctuations and the finite bandwidth of the dominant lines in the Fourier transform representation of the shock-cell structure.

The remaining BBSAN prediction results are presented in order of increasing M_j and then the associated TTR as shown in Table 1. Using the same NPR as the previous case, heating is added to the converging nozzle flow at a TTR = 2.20. The BBSAN predictions are shown in Fig. 5. Overall, the spectral shape of the predictions is excellent and the peaks of each BBSAN component are captured. In earlier predictions, the levels were overpredicted by approximately 6 dB. This was before Tam's [9] temperature correction, Eq. (27), was used. Tam [9] argued that as the jet temperature increases, for supersonic conditions, the growth rate and amplitude of the large-scale turbulent structures should decrease. This is supported by instability theory. Thus, it is expected that the turbulence levels should decrease as the jet temperature increases. This is not found in

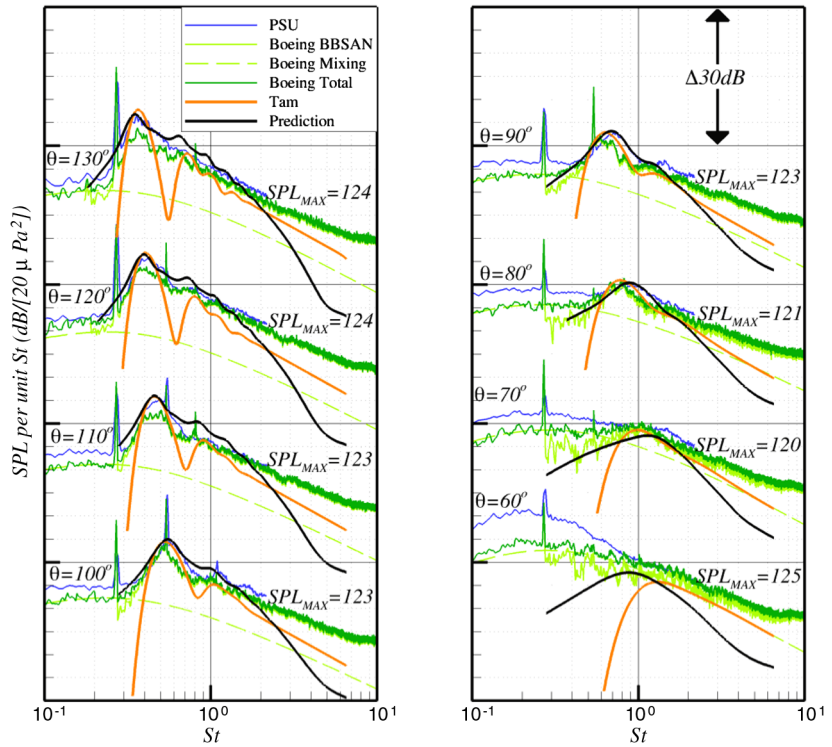

Fig. 5 Comparisons of BBSAN predictions with experiments for $M_d = 1.00$, $M_j = 1.50$, TTR $= 2.20$, and $R/D = 100$.

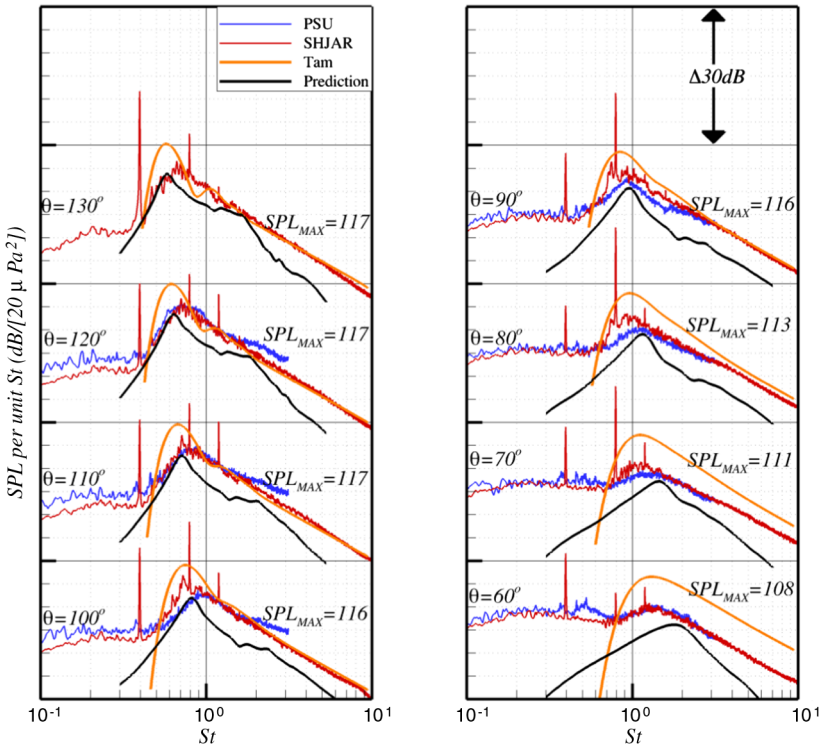

Fig. 6 Comparisons of BBSAN predictions with experiments for $M_d = 1.50$, $M_j = 1.30$, TTR = 1.00, and $R/D = 100$.

either the K-Ω or K-ε RANS simulations. In the absence of an improved RANS turbulence model for the effect of jet heating, Tam's correction factor has been adopted here as an empirical correction for the effects of jet heating. Turbulence modeling may be one of the issues that contributes to the poor scaling of the BBSAN intensity with increasing TTR. It could also be attributed to a failure to capture this phenomena with the acoustic model. The reason why the BBSAN intensity does not continue to increase with increasing TTR beyond a threshold value is not understood and is a topic of current research.

Two overexpanded cases of $M_d = 1.50$, $M_j = 1.30$, and TTR = 1.00 and TTR = 2.20 are shown in Figs. 6 and 7, respectively. In the unheated case the peak levels are underpredicted and the spectral peaks are somewhat narrower than in the experiments. In the heated case, there is good agreement between the predictions and the experiments. In the unheated case the BBSAN is evident at all angles to the jet axis. However, in the heated case, the mixing noise is clearly dominant at angles less than 80 deg to the jet downstream axis. There is also close agreement between the present predictions and Tam's [9] model in the heated case. In the unheated case, Tam's model

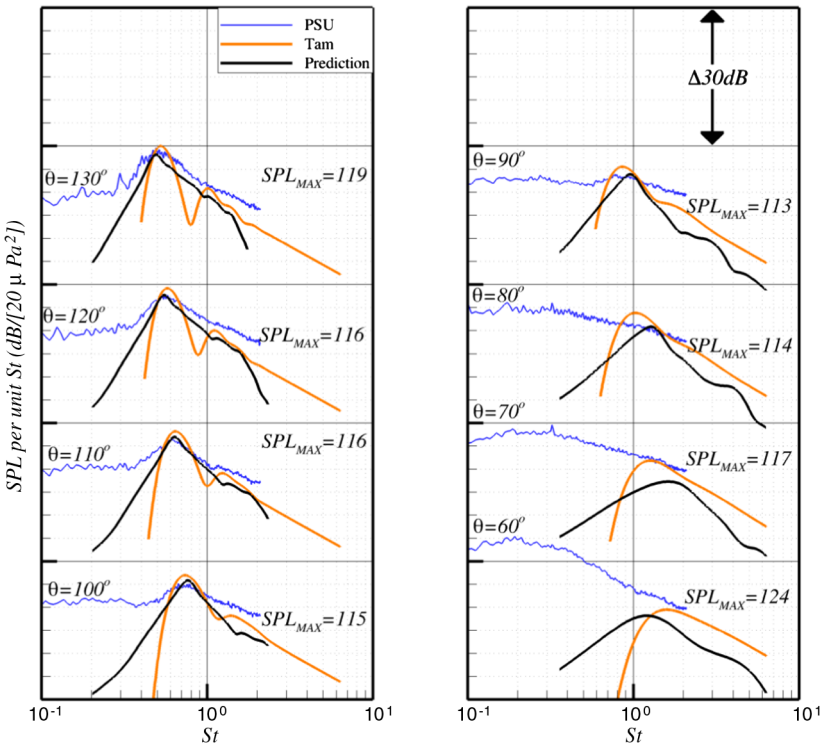

Fig. 7 Comparisons of BBSAN predictions with experiments for $M_d = 1.50$, $M_j = 1.30$, TTR = 2.20, and $R/D = 100$.

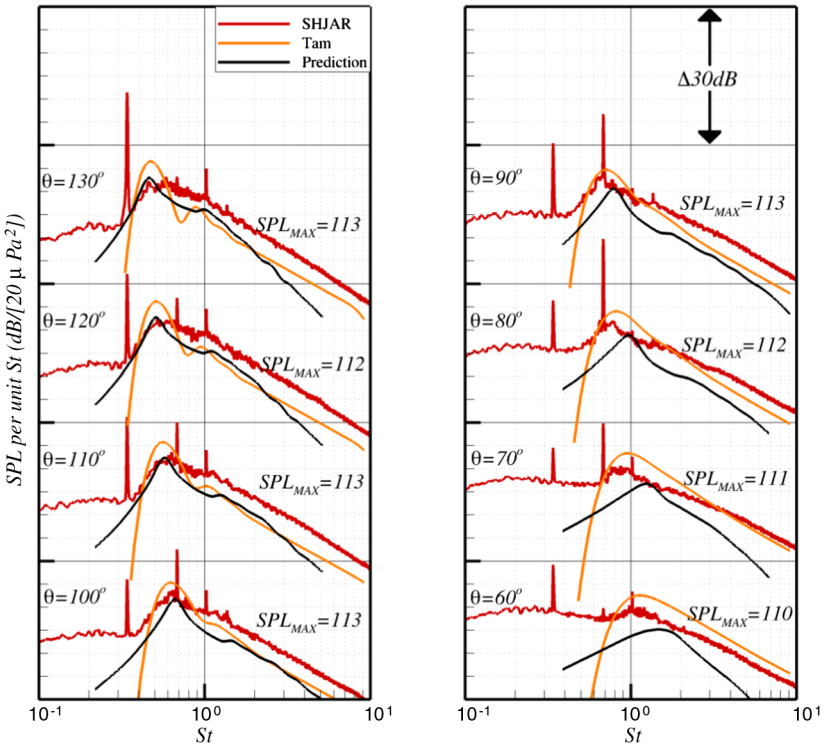

Fig. 8 Comparisons of BBSAN predictions with experiments for $M_d = 1.50$, $M_j = 1.40$, TTR = 1.00, and $R/D = 100$.

overpredicts the levels, whereas the present model underpredicts them slightly.

Two slightly offdesign cases have been predicted with over- and underexpanded jets for $M_d = 1.50$ and TTR = 1.00. Predictions for jets with $M_j = 1.40$ and 1.60 are presented in Figs. 8 and 9, respectively. SHJAR data at $M_j = 1.38$ and 1.61, as well as predictions using Tam's [4] model are also shown. The general shape of the dominant BBSAN peak agrees well between the two prediction schemes, with the current implementation having a slightly narrower peak. When the observer angle is less than $\theta = 90°$, the present prediction scheme gives levels that are lower than the peaks predicted by Tam's model. However, the overall amplitude of Tam's model at larger observer angles is generally higher than the measurements in the overexpanded case and similar to the measurements in the underexpanded case. The present predictions give the correct amplitude in the overexpanded case and are too low in the underexpanded case.

In the predictions presented thus far, the peak magnitude of BBSAN decreases in the downstream direction of the jet and increases slightly as the observer angle moves towards the upstream

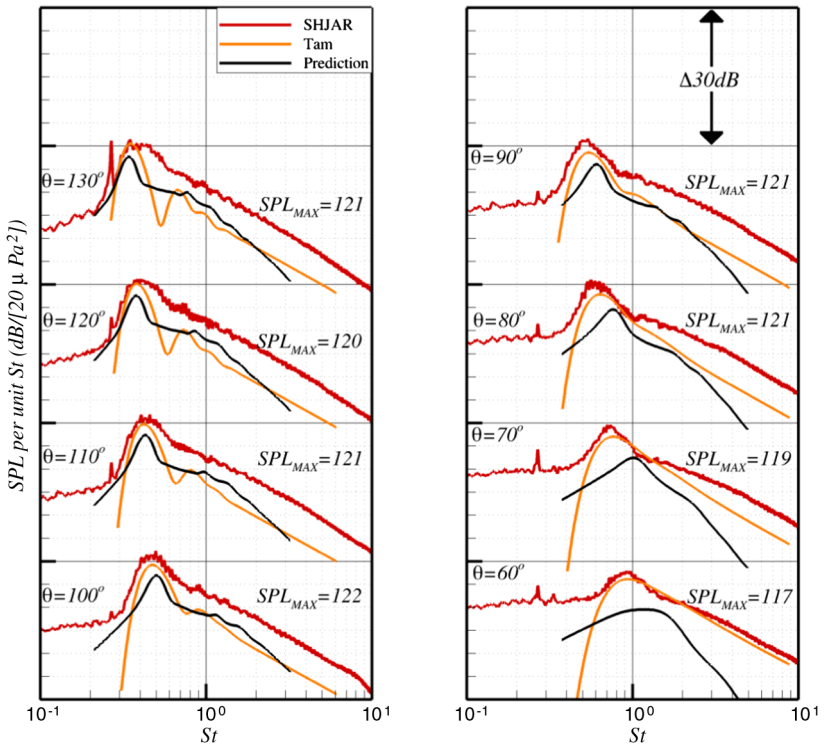

Fig. 9 Comparisons of BBSAN predictions with experiments for $M_d = 1.50$, $M_j = 1.60$, TTR = 1.00, and $R/D = 100$.

Table 2 Jet operating conditions for the RANS CFD and BBSAN predictions for the rectangular jet.

M_d	M_j	NPR	TTR	D_e, m	D_{ej}, m	f_c	β	T_j, K	U_j, m/s
1.50	1.30	2.77	1.00	0.01778	0.0184	21,001	0.749	219.0	385.6
1.50	1.70	4.94	1.00	0.01778	0.0206	22,581	0.801	185.6	464.4
1.50	1.30	2.77	2.20	0.01778	0.0184	31,150	0.749	481.8	571.9
1.50	1.70	4.94	2.20	0.01778	0.0206	33,493	0.801	408.4	688.9

direction. This agrees with experimental data and the BBSAN components shown by Viswanathan et al. [18]. This behavior is shown by the present predictions with a model that does not include the influence of the mean flow refraction effects on the BBSAN. Miller and Morris [20] show that the mean flow effects in dual-stream jets for sources in the outer shear layer are negligible. However, mean flow effects cannot be ignored for the inner shear layer, as sound from these sources must propagate through the outer high-speed stream. This effect is included by Tam et al. [21] in their extension of Tam's [4] BBSAN model to dual-stream jets.

B. Single-Stream Rectangular Jet

To demonstrate the use of the BBSAN prediction model in three-dimensional jets, both unheated and heated rectangular jets have been considered. In this case both the CFD solution and the source integration must be conducted in three dimensions. The operating conditions examined are given in Table 2. Results are only shown for the underexpanded case.

The unheated and heated rectangular-jet CFD calculations with $M_d = 1.5$ were validated by comparisons with schlieren visualizations [22]. The rectangular nozzle chosen has $M_d = 1.50$, based on area ratio, and operates either over- or underexpanded with $M_j = 1.30$ or $M_j = 1.70$ and TTR = 1.00 or TTR = 2.20. The experimental results are documented in Veltin and McLaughlin [23] and Goss et al. [24]. The nozzle exit width and height are 0.0208 m and 0.0119 m, respectively, giving an aspect ratio of 1.75. Microphones were placed at 1.905 m from the jet at various polar and azimuthal angles. The experimental data were extended to 100 D_e, where D_e is the equivalent diameter of the rectangular jet, to be consistent with the axisymmetric jet predictions presented in the previous section. The characteristic frequencies of the rectangular jets are based on the fully expanded equivalent diameter D_{ej} found from D_e and NPR.

Unlike the axisymmetric version of the code, the three-dimensional BBSAN implementation evaluates the integrals over three-dimensional source and wave-number integration regions. Since there is an additional integral that needs to be evaluated in the z direction, the run time of the computer code can increase greatly. To reduce the execution time, careful choices are made of the range and number of indices for the integration. Based on the conclusions for the integration studies for the axisymmetric jet, source integration ranges for the four rectangular cases are chosen as 0.001 m$< x <$ 0.1437 m, 0.001 m $< y <$ 0.011 m, and 0.001 m $< z <$ 0.021 m with grid index values of 300, 75, and 75, respectively. Since the RANS CFD simulations use planes of symmetry of the nozzle, the implemented BBSAN code automatically integrates across these planes. There is no restriction in the implemented version of the BBSAN model regarding the flowfield, even though planes of symmetry were used to construct the RANS solution. The same implementation of BBSAN can be applied to any three-dimensional jet flowfield. The range of the wave-number integration region is chosen as 0.001 m $< x <$ 0.250 m with 512 grid points. Evaluation of Eq. (36) only includes contributions from regions where K exceeds 10% of its maximum value. The solution is found relatively quickly by specifying a limited range for the wave-number integrations to only encompass peak values of the wave-number spectrum. For example, the wave-number resolution is given by $\Delta k = 12.57$ m^{-1}, and only wave-number contributions in the range of -25 m$^{-1} > k > -166$ m^{-1} and 25 m$^{-1} < k <$ 166 m^{-1} are used.

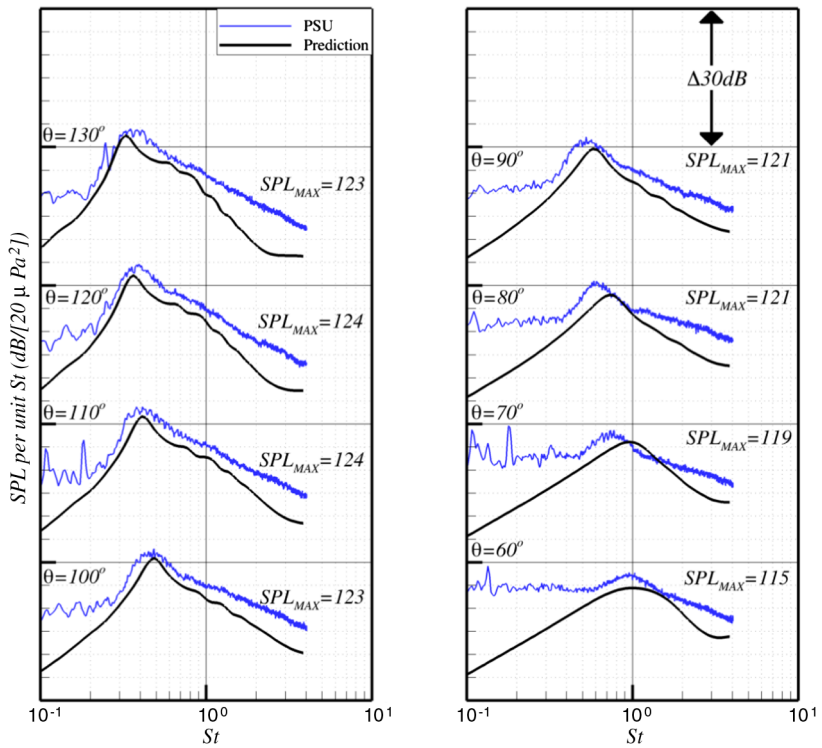

Fig. 10 Comparisons of BBSAN predictions with experiments for the rectangular jet $M_d = 1.50, M_j = 1.70$, TTR = 1.00, and $R/D_e = 100$ in the minor-axis direction.

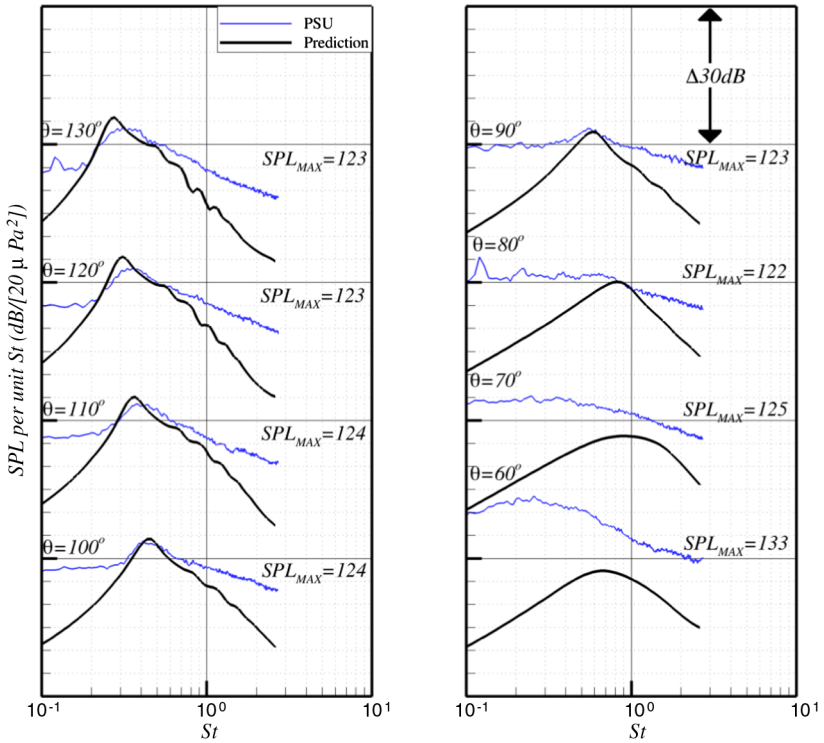

Fig. 11 Comparisons of BBSAN predictions with experiments for the rectangular jet $M_d = 1.50, M_j = 1.70$, TTR $= 2.20$, and $R/D_e = 100$ in the minor-axis direction.

Figure 10 shows predictions for the underexpanded unheated rectangular jet operating at $M_j = 1.70$ in the minor-axis plane. In this case, the magnitude of the BBSAN is invariant with azimuthal angle. The predictions at all observer angles align with those of the experiment. The first BBSAN peak and subsequent minor peaks at higher frequencies generally align with those of experiment. Figure 11 shows predictions for the heated underexpanded rectangular jet with $M_j = 1.70$ and TTR $= 2.20$. The peak frequencies match those of the experiment very well at most angles except for larger observer angles, though the agreement is still quite good. At low observer angles the BBSAN is much weaker than the mixing noise, since the jet is heated. The predicted values of BBSAN do not contribute to the total spectra, just as in the corresponding heated-circular-jet case.

V. Conclusions

A BBSAN prediction model has been developed that requires only the specification of the operating conditions and geometry of the nozzle. The RANS CFD solution is the only input required by the BBSAN model. A vector Green's function is used to find the acoustic pressure in the far field from the compressible linearized Euler equations. The final prediction formula involves an integration over the BBSAN source region and an axial wave number. The model can be applied to any kind of jet flowfield, nozzle shape, offdesign parameter, or temperature ratio. An exponential/Gaussian model for the two-point cross-correlation of the turbulent velocity fluctuations is used. The model does require values for the turbulent length and time scales as a function of spatial position. These values are linked to the RANS CFD simulation by simple formulas and scaling coefficients.

The BBSAN model has been used to conduct parametric studies of the source and wave-number integration regions, including grid density studies of these regions, to obtain grid-independent solutions. The model has been calibrated by adjusting the scaling coefficients that represent the relevant turbulent length and times scales at one operating condition only. These coefficients are only calibrated against the single operating condition of a cold underexpanded jet. The scaling coefficients have not been optimized for a wide range of jet conditions. This optimization has not been performed in order to help better illustrate the model's capability. An example of a recalibration of the model based on a heated jet case without screech is given in Appendix A.

A wide range of calculations of single-stream jets with various M_d, M_j, and TTR have been chosen to test the BBSAN model and its implementation. Selective integration over small ranges of the axial wave-number region has shown how the peaks of the wave-number spectrum contribute to different peaks in the predicted BBSAN spectral density. The effect of jet heating is to increase the noise levels, for the same NPR, by 5–6 dB for a TTR $= 2.20$ compared to the unheated case. This can be associated with a jet velocity scaling given by U_j^3. However, the measured experimental changes are smaller and do not change beyond a moderate amount of heating. A temperature correction factor suggested by Tam [9] has been implemented for all predictions, heated and unheated. This adjustment does not change the shape of the spectrum, it only changes its amplitude. The general form of the BBSAN model developed is fully three-dimensional and has been used for rectangular-jet noise predictions. These predictions compare very favorably with measurements.

Though the present BBSAN model has been shown to be very successful, there are improvements that could be made. It is possible that the predictions at high frequencies could be improved by adding a frequency dependence to the characteristic turbulent length scale l. Experimental data show that the length scale decreases with increasing frequency, whereas it remains constant in the model. In addition, the assumed form for the two-point cross-correlation function of the turbulent velocity fluctuations is exponential/Gaussian in nature and is based on similar forms used in the prediction of turbulent mixing noise. However, the components of the turbulence that are most important for BBSAN are the large-scale coherent structures. The statistical properties of these structures would be expected to show significant positive and negative peaks in their cross-correlations. The effects of changes in the model for the turbulent velocity cross-correlation could be examined. Furthermore, the cross-stream length scale has been assumed to be independent of separation direction. So the prediction formula could be further improved by allowing for a dependence on separation

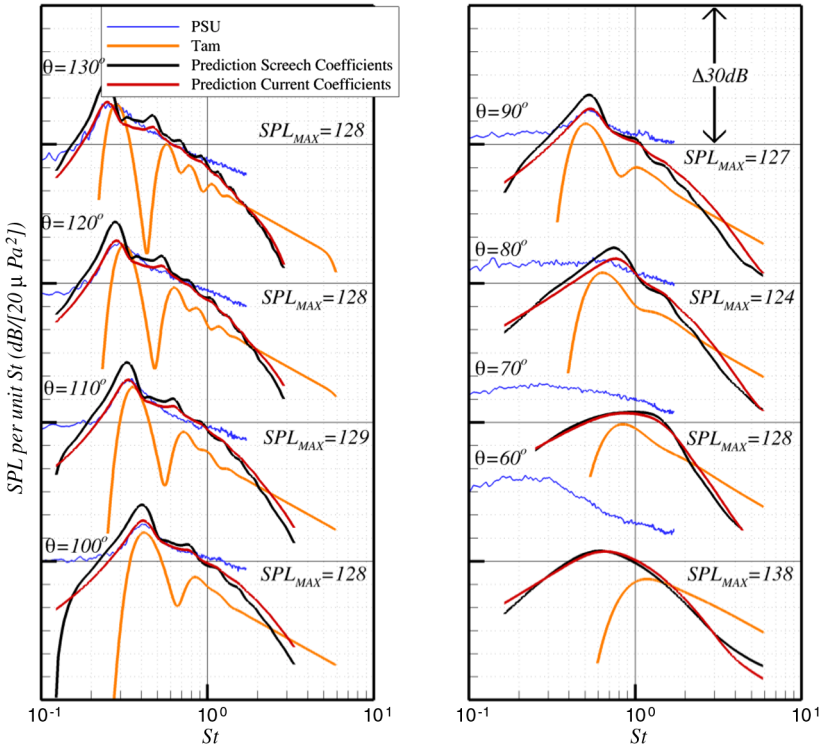

Fig. A1 Comparisons of BBSAN predictions using turbulence coefficients that are optimized for a nonscreeching jet with experiments for $M_d = 1.50$, $M_j = 1.70$, TTR $= 2.20$, and $R/D = 100$.

direction, thus improving predictions for highly three-dimensional flowfields with anisotropic turbulent length scales in the cross-stream direction. A near-field prediction formula should also be developed so that the model can be implemented in noise prediction codes that take into account scattering by the aircraft structures. Near-field noise is also important for structural loading estimates as well as sound transmission studies for both civilian and military aircraft. A vector Green's function could be evaluated numerically rather than assuming that propagation effects through the mean flow are not negligible. This is likely to be most important for dual-stream jets, where the BBSAN from the primary jet must propagate through the secondary stream. Preliminary dual-stream jet calculations have been made by the authors, and there is evidence that the presence of the high-speed secondary stream does affect the predicted directivity (see also Tam [21]).

Appendix A: Effect of Calibration Constants

The coefficients, c_τ, c_l, and $c_\perp$, have been calibrated for a $M_d = 1.00$, $M_j = 1.50$, and TTR $= 1.00$ jet at $\theta = 100°$. These coefficients, the associated amplitude scaling factor P_f, and the temperature correction, have been used to make all predictions shown in this paper. The same coefficients are used for each observer angle, nozzle geometry, and jet conditions creating a true prediction scheme. However, screech tones are very evident in the jet spectra (see Fig. 3). Screech is not often found in heated jets or on full-scale scale engines. To examine the effects of a different choice of coefficients, their values have been determined for the $M_d = 1.50$, $M_j = 1.70$, and TTR $= 2.20$ jet. The angle chosen for calibration is $\theta = 100°$ as before. The best coefficients for a jet without screech are given by $c_\tau = 0.85$, $c_l = 3.00$, $c \perp = 0.30$, and $P_f = 101.3$. These coefficients yield good predictions for a wide range of jets without screech. Figure A1 shows predictions for the $M_d = 1.50$, $M_j = 1.70$, and TTR $= 2.20$ jet at $R/D = 100$. Experimental data from PSU, Tam's [4] model, and two BBSAN predictions are shown. The black line shows BBSAN predictions using the original coefficients, $c_\tau = 1.25$, $c_l = 3.25$, $c \perp = 0.30$, which were calibrated for the screeching jet operating at $M_d = 1.00$, $M_j = 1.50$, and TTR $= 1.00$. The predictions using the new coefficients are shown in red. Since the jet is heated the temperature correction factor has been applied to both BBSAN predictions. Use of the new coefficients to predict the BBSAN shows that more precise scaling is captured of the variation of BBSAN with observer angle, the peak BBSAN magnitudes are captured successfully, and the width of the primary and sometimes secondary BBSAN peaks matches the experimental data successfully.

References

[1] Harper-Bourne, M., and Fisher, M. J., "The Noise from Shock Waves in Supersonic Jets," *AGARD Conference on Noise Mechanisms*, CP-131, AGARD, Brussels, Belgium, 19–21 Sept. 1973, pp. 11.3–11.13.

[2] "Gas Turbine Jet Exhaust Noise Prediction," Rev. D, SAE International, Rept. SAE ARP876, Warrendale, PA, 1994.

[3] Zorumski, W. E., "Aircraft Noise Prediction Program. Theoretical Manual," Pts. 1, 2, NASA TM 83199, 1982.

[4] Tam, C. K. W., "Stochastic Model Theory of Broadband Shock Associated Noise from Supersonic Jets," *Journal of Sound and Vibration*, Vol. 16, No. 2, 1987, pp. 265–302.

[5] Tam, C. K. W., and Tanna, H. K., "Shock-Associated Noise of Supersonic Jets from Convergent–Divergent nozzles," *Journal of Sound and Vibration*, Vol. 81, No. 3, 1982, pp. 337–358. doi:10.1016/0022-460X(82)90244-9

[6] Pack, D. C., "A Note on Prandtl's Formula for the Wavelength of a Supersonic Gas Jet," *Quarterly Journal of Applied Mathematics and Mechanics*, Vol. 3, 1950, pp. 171–181.

[7] Tam, C. K. W., Jackson, J. A., and Seiner, J. M., "A Multiple-Scales Model of the Shock-Cell Structure of Imperfectly Expanded Supersonic Jets," *Journal of Fluid Mechanics*, Vol. 153, 1985, pp. 123–149. doi:10.1017/S0022112085001173

[8] Tam, C. K. W., and Chen, K. C., "A Statistical Model of Turbulence in Two-Dimensional Mixing Layers," *Journal of Fluid Mechanics*, Vol. 92, 1979, pp. 303–326. doi:10.1017/S002211207900063X

[9] Tam, C. K. W., "Broadband Shock-Associated Noise of Moderately Imperfectly Expanded Supersonic Jets," *Journal of Sound and Vibration*, Vol. 140, No. 1, 1990, pp. 55–71. doi:10.1016/0022-460X(90)90906-G

[10] Lele, S. K., "Phased Array Models of Shock-Cell Noise Sources," AIAA Paper 2005-2841, 2005.

[11] Shur, M. L., Spalart, P. R., and Strelets, M. K., "Noise Prediction for Increasingly Complex Jets. Part I: Methods and Tests," *International*

Journal of Aeroacoustics, Vol. 4, Nos. 3–4, 2005, pp. 213–246.
doi:10.1260/1475472054771376

[12] Shur, M. L., Spalart, P. R., and Strelets, M. K., "Noise Prediction for Increasingly Complex Jets. Part II: Applications," *International Journal of Aeroacoustics*, Vol. 4, Nos. 3–4, 2005, pp. 247–266.
doi:10.1260/1475472054771385

[13] Ray, P. K., "Sound Generated by Instability Wave/Shock-Cell Interaction in Supersonic Jets," *Journal of Fluid Mechanics*, Vol. 587, 2007, pp. 173–215.

[14] Tam, C. K. W., and Auriault, L., "Mean Flow Refraction Effects on Sound Radiated from Localized Sources in a Jet," *Journal of Fluid Mechanics*, Vol. 370, 1998, pp. 149–174.
doi:10.1017/S0022112098001852

[15] Nelson, C., "An Overview of the NPARC Alliance's Wind-US Solver," AIAA Paper 2010-0027, 2010.

[16] Menter, F. R., "Two-Equation Eddy-Viscosity Turbulence Models for Engineering Applications," *AIAA Journal*, Vol. 32, No. 8, 1994, pp. 1598–1605.
doi:10.2514/3.12149

[17] Miller, S. A. E., Veltin, J., Morris, P. J., and McLaughlin, D. K., "Assessment of Computational Fluid Dynamics for Supersonic Shock Containing Jets," *AIAA Journal*, Vol. 47, No. 11, 2009, pp. 2738–2746.
doi:10.2514/1.44336

[18] Viswanathan, K., Alkislar, M. B., and Czech, M. J., "Characteristics of the Shock Noise Component of Jet Noise," *AIAA Journal*, Vol. 48, No. 1, 2010, pp. 25–46.
doi:10.2514/1.38521

[19] Viswanathan, K., "Scaling Laws and a Method for Identifying Components of Jet Noise," *AIAA Journal*, Vol. 44, No. 10, 2006, pp. 2274–2285.
doi:10.2514/1.18486

[20] Miller, S. A. E., and Morris, P. J., "The Prediction of Broadband Shock-Associated Noise from Dual Stream and Rectangular Jets Using RANS CFD," AIAA Paper 2010-3730, 2010.

[21] Tam, C. K. W., Pastouchenko, N., and Viswanathan, K., "Broadband Shock-Cell Noise from Dual Stream Jets," *Journal of Sound and Vibration*, Vol. 324, 2009, pp. 861–891.
doi:10.1016/j.jsv.2009.02.012

[22] Miller, S. A. E., "The Prediction of Broadband Shock-Associated Noise Using Reynolds-Averaged Navier-Stokes Solutions," Ph.D. Thesis, Pennsylvania State Univ., University Park, PA, 2009.

[23] Veltin, J., and McLaughlin, D., "Flowfield and Acoustic Measurements of Rectangular Supersonic Jets," AIAA Paper 2009-0019, 2009.

[24] Goss, A. E., Veltin, J., Lee, J., and McLaughlin, D. K., "Acoustic Measurements of High-Speed Jets from Rectangular Nozzle with Thrust Vectoring," *AIAA Journal*, Vol. 47, No. 6, 2009, pp. 1482–1506.
doi:10.2514/1.39843

A. Lyrintzis
Associate Editor